

The outer low- α disc of the Milky Way – I: evidence for the first pericentric passage of Sagittarius?

Payel Das¹,  ¹★ Yang Huang,^{2,3} Ioana Ciucă^{4,5,6} and Francesca Fragkoudi^{7,8}

¹*Astrophysics Research Group, University of Surrey, Guildford, Surrey, GU2 7XH, UK*

²*School of Astronomy and Space Science, University of Chinese Academy of Sciences, Beijing 100049, P. R. China*

³*Key Lab of Optical Astronomy, National Astronomical Observatories, Chinese Academy of Sciences, Beijing 100012, P. R. China*

⁴*Research School of Astronomy & Astrophysics, Australian National University, Canberra, ACT 2611, Australia*

⁵*School of Computing, Australian National University, Canberra, ACT 2601, Australia*

⁶*ARC Centre of Excellence for All Sky Astrophysics in 3 Dimensions (ASTRO 3D), Australia*

⁷*Institute for Computational Cosmology, Durham University, South Road, Durham DH1 3LE, UK*

⁸*Department of Physics, Durham University, South Road, Durham DH1 3LE, UK*

Accepted 2023 October 27. Received 2023 October 26; in original form 2023 June 8

ABSTRACT

Phase-space data, chemistry, and ages together reveal a complex structure in the outer low- α disc of the Milky Way. The age-vertical velocity dispersion profiles beyond the Solar Neighbourhood show a jump at 6 Gyr for stars beyond the Galactic plane. Stars older than 6 Gyr are significantly hotter than younger stars. The chemistry and age histograms reveal a bump at $[\text{Fe}/\text{H}] = -0.5$, $[\alpha/\text{Fe}] = 0.1$, and an age of 7.2 Gyr in the outer disc. Finally, viewing the stars beyond 13.5 kpc in the age-metallicity plane reveals a faint streak just below this bump, towards lower metallicities at the same age. Given the uncertainty in age, we believe these features are linked and suggest a pericentric passage of a massive satellite ~ 6 Gyr ago that heated pre-existing stars, and led to a starburst in existing gas. New stars also formed from the metal-poorer infalling gas. The impulse approximation was used to characterize the interaction with a satellite, finding a mass of $\sim 10^{11} M_{\odot}$, and a pericentric position between 12 and 16 kpc. The evidence points to an interaction with the Sagittarius dwarf galaxy, likely its first pericentric passage.

Key words: methods: data analysis – surveys – Galaxy: abundances – Galaxy: disc – Galaxy: kinematics and dynamics.

1 INTRODUCTION

The third data release of *Gaia* has given us access to parallaxes and proper motions for a billion stars (Gaia Collab. et al. 2016; Arenou et al. 2018; Gaia Collab. et al. 2018; Lindegren et al. 2018; Gaia Collab. et al. 2021). Millions of these stars have complementary spectroscopic data from a range of surveys, for which ages and distances have been estimated using isochrones (e.g. Mints & Alexey 2018; Queiroz et al. 2018; Sanders & Das 2018; Kordopatis et al. 2023), and ages have been estimated for red giant samples using data-driven spectroscopic estimators (Das & Sanders 2019; Huang et al. 2020; Ciucă et al. 2021). Six-dimensional phase-space coordinates, metallicity, a number of abundances, and age have thus become available for an extraordinary number of stars, enabling us to characterize the chemodynamical behaviour of stars in detail both within the Solar Neighbourhood and beyond. The outer disc of the Milky Way has been revealed to unprecedented detail for the first time.

The low- $[\alpha/\text{Fe}]$ stars in our Milky Way have been shown to flare, i.e. the vertical scale height of the stars increases with radius (e.g. Bovy et al. 2016; Thomas et al. 2019; Yu et al. 2021). The scale height varies by a factor of two between the Solar Neighbourhood

and a Galactocentric distance of 12 kpc (Amôres, Robin & Reylé 2017). It exists across all ages and is more pronounced for the metal-poorer ($[\text{Fe}/\text{H}] \sim -0.6$) stars (Mackereth et al. 2017). The radial velocity dispersion profile falls exponentially throughout for the oldest stars, while the youngest stars plateau beyond the solar radius (Sanders & Das 2018; Sharma et al. 2021). The vertical velocity dispersion profile falls exponentially until just beyond the solar radius and then plateaus for the oldest stars and even rises again for the youngest stars. This is partially attributable to a selection function effect, as stars at a larger heliocentric distance will be observed at higher vertical heights and are therefore likely to have higher vertical velocity dispersions. However, one may also expect a flat vertical velocity dispersion, under the assumption of approximate equilibrium. If we imagine the vertical structure of the outer disc to be approximately described by vertical slab dynamics, then the vertical velocity dispersion is proportional to the dependence of the vertical height on Galactocentric radius, multiplied by the slope of the circular velocity curve. The vertical height increases roughly as R , and the circular velocity curve is dominated by dark matter, which decreases roughly as $1/R$ for an NFW profile. Therefore, the vertical velocity dispersion profile should be approximately constant.

The flare in the outer low- $[\alpha/\text{Fe}]$ disc could be a consequence of the radial migration of stars from the inner disc. Minchev et al. (2012a) investigated the evolution of galactic discs in N -body simulations. They found that the outskirts of discs comprised of stars migrated

* E-mail: p.das@surrey.ac.uk

from the inner disc would have relatively large radial velocity dispersions. However, other work (Minchev et al. 2012b; Vera-Ciro et al. 2014; Vera-Ciro & D’Onghia 2016) found that inward migrators thin down as they move in, whereas outward migrators preserve the disc scale height at their destination.

Flaring has also been shown in a number of N -body simulations to result from interactions between the disc and satellites (Velazquez & White 1999; Kazantzidis et al. 2009; Gómez et al. 2013; García de la Cruz et al. 2020). Martig, Minchev & Flynn (2014a) studied seven simulated disc galaxies, three with a quiescent merger history, and four with mergers in the last 9 Gyr. All galaxies undergo a phase of merging activity at high redshift, so that stars older than 9 Gyr are found in a centrally concentrated component, while younger stars are mostly found in discs. They find that the lack of flaring did not necessarily imply a merger-free history, but mergers produce discontinuities between thin and thick disc components, and jumps in the age-velocity relation (Martig, Minchev & Flynn 2014b). Exploration of chemodynamical data in LAMOST, SEGUE, APOGEE, and *Gaia* surveys has also found evidence for phase-mixed stars in the outer disc kicked up by impacts with early satellite interactions (Laporte et al. 2020; Horta et al. 2023), as well as those in the process of phase mixing from more recent satellite interactions (Laporte, Koposov & Belokurov 2022).

Church, Mocz & Ostriker (2019) compared the heating effect of ultralight axion-like particles or ‘fuzzy dark matter (FDM)’ to cold dark matter (CDM) subhaloes. They found that both produce a flaring that terminates the Milky Way disc at 15–20 kpc. Chiang, Ostriker & Schive (2023) present a more sophisticated treatment that incorporates the full baryon and dark matter distributions of the Milky Way, and adopts stellar disc kinematics inferred from recent *Gaia*, APOGEE, and LAMOST surveys. They found that repeated subhalo passages drives flaring of the outer disc and can even result in the observed ‘U-shaped’ disc vertical velocity dispersion profile (Sanders & Das 2018).

Renaud et al. (2021b) find in VINTERGATAN, a cosmological simulation of a Milky-Way-like galaxy, that the outer gas disc is fuelled by a distinct metal-poorer gas flow to the inner disc. The first passage of the last major merger galaxy triggers star formation. These *in situ* stars have halo-like kinematics, due to the inclination of the outer disc that eventually aligns with the inner one via gravitational torques, therefore simulating a flared disc.

Here, we use a sample of $\sim 140\,000$ primary red clump (RC) stars drawn from the Large Sky Area Multi-Object fiber Spectroscopic Telescope (LAMOST) survey (Huang et al. 2020), which have precise distances and proper motions from *Gaia* DR3, and machine-learned ages. This group of stars uniquely comprises primarily flared thin-disc stars, as they are metal rich, and belong to the Galactic anticentre. We select low- α stars, and explore their phase-space, chemical, and age structure in Section 2. We calculate robust vertical velocity dispersion profiles in Section 3. We find evidence for a jump in the vertical velocity dispersion at 6 Gyr, for stars in the outer disc and beyond the Galactic plane. We attribute this to an interaction with a massive satellite, and characterize its position and mass using the impulse approximation in Section 4. We discuss our results in the context of relevant literature in Section 5, and conclude in Section 6.

2 PHASE-SPACE, CHEMICAL, AND AGE STRUCTURE

Here, we explore the structure of the data in phase space, chemistry, and age. We adopt a left-handed coordinate system in which positive v_R points away from the Galactic Centre and positive

v_ϕ points in the direction of Galactic rotation. To convert from Equatorial coordinates to Galactocentric coordinates, we assume that the Sun is located at $(R_0, z_0) = (8.2, 0.014)$ kpc (McMillan 2017), that the Local Standard of Rest (LSR) has an azimuthal velocity of 232.8 km s^{-1} , and that the velocity of the Sun relative to the LSR is $(v_R, v_\phi, v_z) = (-8.6, 13.9, 7.1) \text{ km s}^{-1}$ (McMillan 2017).

2.1 The data

Huang et al. (2020) select stars with spectral signal-to-noise ratios higher than 20 from the 4th release of the LAMOST Galactic spectroscopic surveys. The selection is based on their positions in the metallicity-dependent effective temperature–surface gravity and colour–metallicity diagrams, supervised by high-quality Kepler asteroseismology data.

The stellar masses and ages of the primary RC stars are determined using the Kernel Principal Component Analysis method, trained with thousands of RCs in the LAMOST-Kepler fields with accurate asteroseismic mass measurements. Typical uncertainties are 15 and 30 per cent, respectively. The purity and completeness of their primary RC sample are generally higher than 80 per cent. Using over ten thousand primary RCs with accurate distance measurements from parallaxes provided in the 2nd data release from *Gaia*, they recalibrate the K_s absolute magnitudes of primary RCs by considering both the metallicity and age dependencies. With the the new calibration, distances are derived for all the primary RCs, with a typical uncertainty of 5–10 per cent.

We further remove stars from this sample that are likely to be the product of stellar mergers or mass transfer using the following cut (e.g. Sun et al. 2020):

$$[\alpha/\text{Fe}] > 0.12 \text{ and } \tau < 5. \quad (1)$$

These stars need to be removed as their ages would be underestimated due to the additional mass.

2.2 Position, chemistry, and age structure

Fig. 1 shows the positions of the primary RC sample in the $[\alpha/\text{Fe}]$ – $[\text{Fe}/\text{H}]$ plane. The orange line shows a ‘by-eye’ division between the low- and high- α populations. To create our low- α primary RC sample, we select all stars lying below the orange line, which results in a sample of 100 998 stars.

Fig. 2 shows the distribution of the low- α primary RC stars in the R – z plane. The top left plot shows the density map in this plane. The stars reach as far in as $R = 3$ kpc and far out as $R = 20$ kpc at higher z . The sample extends to $z \sim 6$ kpc above and below the mid-Galactic plane. The top right plot shows the $[\text{Fe}/\text{H}]$ map. The metal-rich stars are in the Galactic plane and closer towards the Galactic Centre. There is an asymmetry above and below the plane between 12 and 14 kpc that likely reflects the lines-of-sight selection function evident in the density map (the selection function of the sample will depend on sky positions, colour, and magnitude, and therefore also age and metallicity). The bottom left-hand panel shows the $[\alpha/\text{Fe}]$ map. The stars lowest in $[\alpha/\text{Fe}]$ sit in the Galactic plane. There is no gradient with radius. The bottom right plot shows the age map of the stars, highlighting a young, flaring disc, whose vertical height increases with age and Galactocentric distance. Even though $[\alpha/\text{Fe}]$ is often considered to be a chemical clock, the flare in age is not seen in $[\alpha/\text{Fe}]$. This is likely a result of radial migration (e.g. Sellwood & Binney 2002), bringing together stars born at different radii. Chemical evolution proceeds at different rates at different radii, thus breaking the relation between $[\alpha/\text{Fe}]$ and age.

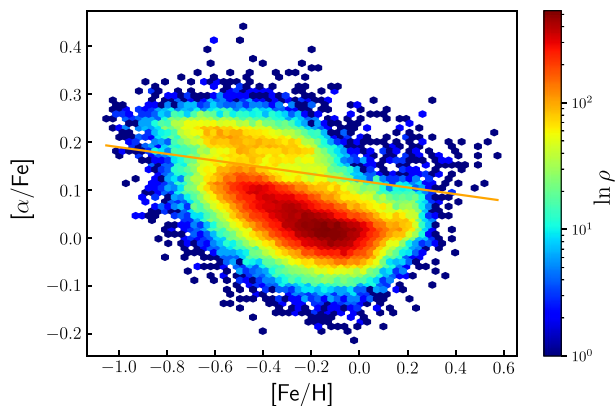


Figure 1. A log-density map of the primary RC sample in the $[\alpha/\text{Fe}]$ – $[\text{Fe}/\text{H}]$ plane. The orange line divides the low- and high- α populations of stars. The low- α primary RC sample contains 108 106 stars.

Fig. 3 plots one-dimensional distributions of the low- α primary RC stars in $[\text{Fe}/\text{H}]$, $[\alpha/\text{Fe}]$, and age, for stars beyond 10, 12, 14, and 16 kpc. A bump emerges that is metal poor, α rich, and about 6 Gyr old, seemingly distinct from another component that is broader in

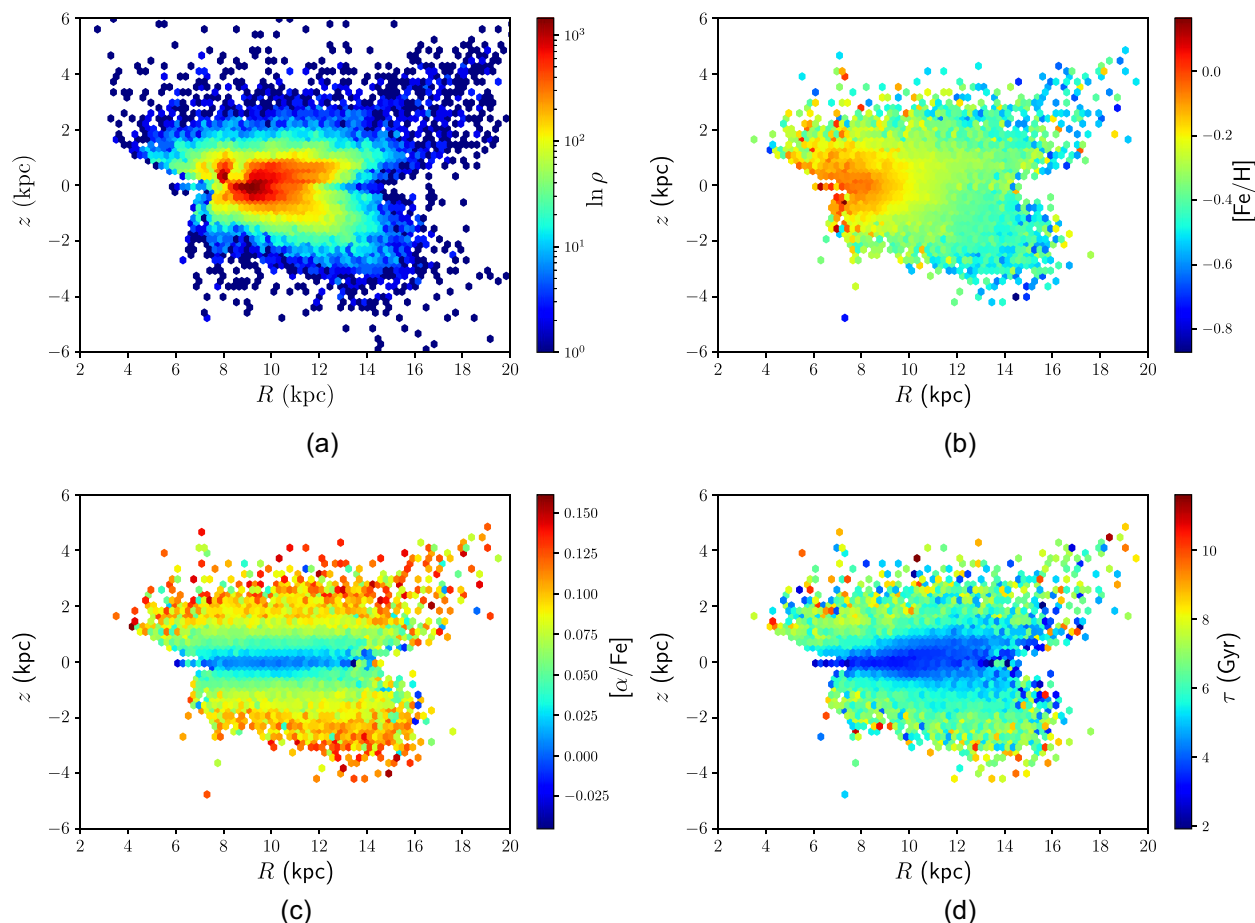


Figure 2. Hexbin plots of the low- α primary RC sample in the R – z plane. The top left-hand panel (a) shows the log-density map, the top right-hand panel (b) shows the $[\text{Fe}/\text{H}]$ map (i.e. each pixel gives a measure of the mean $[\text{Fe}/\text{H}]$ in that R – z region), the bottom left (c) shows the $[\alpha/\text{Fe}]$ map, and the bottom right (d) shows the age map. The sample extends roughly between $3 < R < 16$ kpc and $-6 < z < 6$ kpc. The age distribution highlights a young, flaring disc, whose vertical height increases outwards and with age.

$[\text{Fe}/\text{H}]$, $[\alpha/\text{Fe}]$, and τ . We fit a two-component three-dimensional Gaussian Mixture Model (GMM) to the data beyond 16 kpc finding a narrow component with a mean $[\text{Fe}/\text{H}] = -0.53$, $[\alpha/\text{Fe}] = 0.11$, and $\tau = 7.04$ Gyr and a broad component with a mean $[\text{Fe}/\text{H}] = -0.27$, $[\alpha/\text{Fe}] = 0.04$, and $\tau = 3.84$ Gyr.

3 ROBUST VERTICAL VELOCITY DISPERSION PROFILE

We generate robust vertical velocity dispersion profiles of the low- α primary RC stars, adopting the procedure in Sanders & Das (2018), which allows uncertainties in the velocities to be taken into account. We compute the vertical velocity dispersion of stars in the Galactic plane ($|z| < 0.6$ kpc) and just below and above the Galactic plane ($0.6 < |z| < 1.0$ kpc), separated into 12 radial and 9 age bins in each case. When computing the velocity dispersion in each bin, we account for the uncertainty in each velocity measurement σ_{v_i} in the following way. We first perform a 5σ clip of the raw velocities v_i to remove outliers and halo contaminants. We then seek to maximize the log-likelihood

$$\ln \mathcal{L} = -\frac{1}{2} \sum_i \left(\frac{(v_i - m)^2}{\sigma^2 + \sigma_{v_i}^2} + \ln(\sigma^2 + \sigma_{v_i}^2) \right), \quad (2)$$

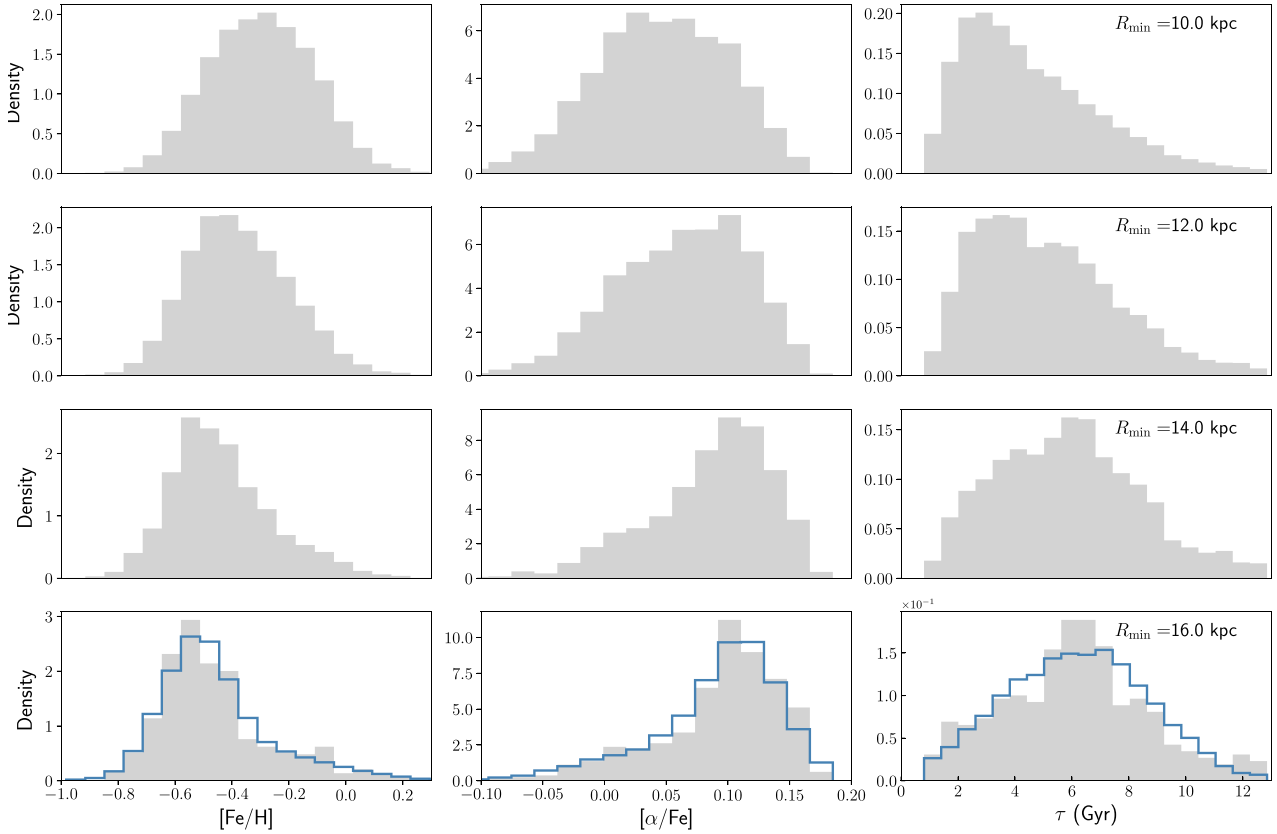


Figure 3. One-dimensional distributions of the low- α primary RC sample in [Fe/H] (left-hand panel), $[\alpha/\text{Fe}]$ (middle panel), and τ (right-hand panel) for stars beyond 10 kpc (top panel), beyond 12 kpc (top middle panel), beyond 14 kpc (bottom middle panel), and beyond 16 kpc (bottom panel). A metal-poor, α -rich, component around 6 Gyr emerges in the very outer disc. The blue histograms show the two-component, three-dimensional GMM fit to the data beyond 16 kpc.

which can be found by solving

$$0 = \sum_i \left(\frac{(v_i - m)^2}{(\sigma^2 + \sigma_{vi}^2)^2} - \frac{1}{\sigma^2 + \sigma_{vi}^2} \right). \quad (3)$$

Here, m is the simple mean computed without accounting for the observational uncertainties. We find the value of σ that solves this equation by Brent’s method (Brent 2013). We estimate the uncertainty on σ from the second derivative of the log-likelihood, approximately given by $\sigma\sqrt{1/2N}$ for N stars.

In the Galactic plane (Fig. 4(a)), the vertical velocity dispersion profiles decrease within ~ 8 kpc before plateauing, with the oldest stars having higher vertical velocity dispersions. Beyond ~ 10 kpc, the vertical velocity dispersion profiles for the youngest stars rise. Above and below the Galactic plane (Fig. 4(b)), the vertical velocity dispersion decreases for all stars until ~ 8 kpc. For stars older than ~ 6 Gyr, the vertical velocity dispersion profile plateaus between ~ 20 to 30 km s^{-1} . The vertical velocity dispersion profile of younger stars continues to fall outwards until ~ 11.5 kpc, where it plateaus. The vertical velocity dispersion profile of stars beyond the Solar Neighbourhood thus appears to ‘jump’ at ~ 6 Gyr. The mean jump amplitude for 6-Gyr stars beyond ~ 11 kpc is $\sim 4 \text{ km s}^{-1}$, greater than the mean error in vertical velocity dispersion of $\sim 1 \text{ km s}^{-1}$ in the same region. The jump is likely only visible beyond the Galactic plane because the survey lines of sight result in a higher density of stars at large radii above and below the plane (see Fig. 2 (a)).

4 THE HEATING EFFECT OF AN INTERACTION WITH A SATELLITE

Here, we examine the possibility that a satellite underwent a pericentric passage with the Milky Way ~ 6 Gyr ago that (i) triggered a starburst in the outer disc producing an overabundance of stars at that time (see Fig. 6), and (ii) heated all pre-existing stars (i.e. stars 6 Gyr old and older) there (see Fig. 4). We generate a mock Milky Way model of the galaxy that is able to describe the vertical velocity dispersion of the stars younger than 6 Gyr, use the impulse approximation to derive the velocity kicks in the case of a Plummer sphere satellite, then show the change to the vertical velocity dispersion profiles of the outer disc stars after a range of different impacts of varying size, concentration, and position.

4.1 A mock Milky Way model

We generate a mock Milky Way with the AGAMA galaxy modelling software (Vasiliev 2019). We use the Milky Way gravitational potential fit in McMillan (2017), generated by thin and thick stellar discs, a H I gas disc, a molecular hydrogen gas disc, and two spheroids representing the bulge and the dark halo. The parameters for their most likely model is given in Table 1.

The densities of the stellar discs are given by

$$\rho_d(R, z) = \frac{\Sigma_0}{2z_d} \exp\left(-\frac{|z|}{z_d} - \frac{R}{R_d}\right), \quad (4)$$

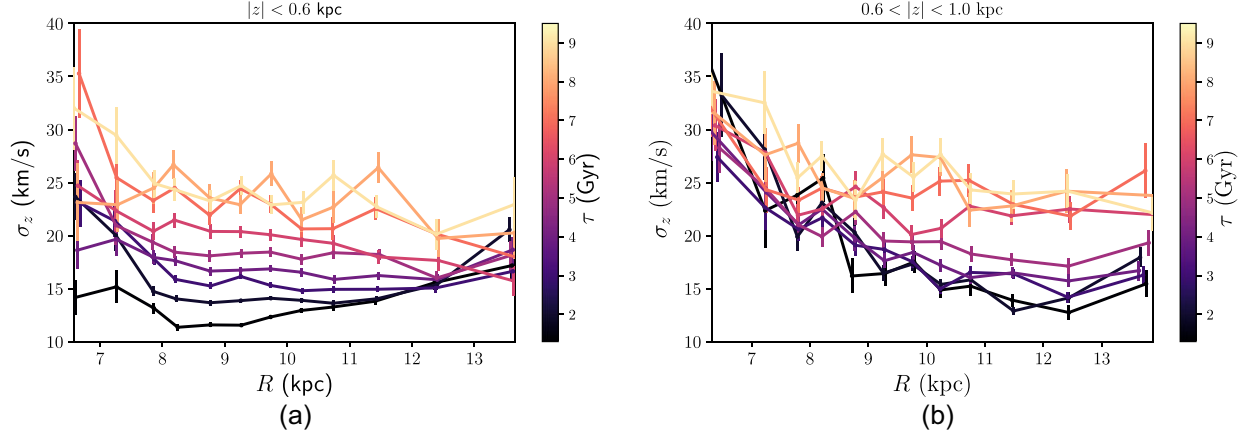


Figure 4. Robust vertical velocity dispersion profiles by age for the low- α primary RC sample in a) the Galactic plane ($|z| < 0.6$ kpc) and b) above and below the Galactic plane ($0.6 < |z| < 1.0$ kpc). All profiles decrease within ~ 8 kpc before plateauing, with the oldest stars having higher vertical velocity dispersions. Beyond ~ 10 kpc, the vertical velocity dispersion profiles for the youngest stars rise. Note the jump in vertical velocity dispersion at 6 Gyr for stars beyond the Solar Neighbourhood, and above and below the Galactic plane.

Table 1. Names, units, values, and descriptions for parameters of the gravitational potential.

	Parameter/Units	Value	Description
Thin disc	$\Sigma_{0, \text{thn}} / (\text{M}_{\odot} \text{ kpc}^{-2})$	8.96×10^8	Central surface density
	$z_{\text{d, thn}} / \text{kpc}$	0.3	Scale height
	$R_{\text{d, thn}} / \text{kpc}$	2.5	Scale radius
Thick disc	$\Sigma_{0, \text{thk}} / (\text{M}_{\odot} \text{ kpc}^{-2})$	1.83×10^8	Central surface density
	$z_{\text{d, thk}} / \text{kpc}$	0.9	Scale height
	$R_{\text{d, thk}} / \text{kpc}$	3.	Scale radius
H I gas disc	$\Sigma_{0, \text{HI}} / (\text{M}_{\odot} \text{ kpc}^{-2})$	5.31×10^7	Central surface density
	$z_{\text{d, HI}} / \text{kpc}$	0.085	Scale height
	$R_{\text{d, HI}} / \text{kpc}$	7.0	Scale radius
	$R_{\text{m, HI}} / \text{kpc}$	4.0	Scale radius of hole
H II gas disc	$\Sigma_{0, \text{HII}} / (\text{M}_{\odot} \text{ kpc}^{-2})$	2.18×10^9	Central surface density
	$z_{\text{d, HII}} / \text{kpc}$	0.045	Scale height
	$R_{\text{d, HII}} / \text{kpc}$	1.5	Scale radius
	$R_{\text{m, HII}} / \text{kpc}$	12.0	Scale radius of hole
Bulge	$\rho_{0, \text{b}} / (\text{M}_{\odot} \text{ kpc}^{-3})$	9.84×10^{10}	Central surface density
	$r_{0, \text{b}} / \text{kpc}$	0.075	Scale radius
	q_{b}	0.5	Axis ratio
	β_{b}	0.0	Inner slope exponent
	γ_{b}	1.8	Outer slope exponent
	$r_{\text{t, b}} / \text{kpc}$	2.1	Truncation radius
Dark matter halo	$\rho_{0, \text{h}} / (\text{M}_{\odot} \text{ kpc}^{-3})$	8.54×10^6	Central surface density
	$r_{0, \text{h}} / \text{kpc}$	19.6	Scale radius
	q_{h}	1.0	Axis ratio
	β_{h}	1.0	Inner slope exponent
	γ_{h}	3.0	Outer slope exponent
	$r_{\text{t, h}} / \text{kpc}$	∞	Truncation radius

with central surface density Σ_0 , scale height z_{d} , and scale length R_{d} . The total mass of each stellar disc is $M_{\text{d}} = 2\pi\Sigma_0 R_{\text{d}}^2$.

The densities of the gas discs are given by

$$\rho_{\text{d}}(R, z) = \frac{\Sigma_0}{4z_{\text{d}}} \exp\left(-\frac{R_{\text{m}}}{R} - \frac{R}{R_{\text{d}}}\right) \text{sech}^2(z/2z_{\text{d}}), \quad (5)$$

with central surface density Σ_0 , scale height z_{d} , and scale length R_{d} . It also has a hole with scale length R_{d} . The mass of each gas disc is

given by $M_{\text{d}} = 2\pi\Sigma_0 R_0 R_{\text{m}} K_2(2\sqrt{R_{\text{m}}/R_{\text{d}}})$, where K_2 is a modified Bessel function.

The densities of the bulge and dark matter halo are given by

$$\rho(R, z) = \frac{\rho_0}{x^{\gamma}(1+x/r_0)^{\beta-\gamma}} \exp[-(x/r_0)^2], \quad (6)$$

where

$$x(R, z) = \sqrt{R^2 + (z/q)^2}. \quad (7)$$

Table 2. Parameter name and units, values, and descriptions for parameters of the thin-disc DF. A dagger indicates the parameter values were taken from Piffl et al. (2014). The remaining parameters (except σ_{\min} , which is introduced in AGAMA) were fit by eye.

Par/Units	Value	Description
R_d / kpc	†2.68	Scale radius
$\tilde{\sigma}_r$ / km s ⁻¹	327.5	Central radial velocity dispersion
$\tilde{\sigma}_z$ / km s ⁻¹	101.6	Central vertical velocity dispersion
$R_{\sigma,r}$ / kpc	3.4	Radial velocity dispersion scale length
$R_{\sigma,z}$ / kpc	5.4	Vertical velocity dispersion scale length
σ_{\min} / km s ⁻¹	1.0	Minimum value of velocity dispersion

ρ_0 sets the density scale, r_0 is a scale radius, and the parameter q is the axis ratio of the isodensity surfaces. The exponents β and γ control the inner and outer slopes of the radial density profile, and r_t is a truncation radius.

For the phase-space distribution of the stars, we assume the action-based quasi-isothermal distribution function (DF) fit to the thin disc in Piffl et al. (2014). The DF for a mono-age stellar population is given by:

$$f(\mathbf{J}) = \frac{\tilde{\Sigma}\Omega}{2\pi^2\kappa^2} \times \frac{\kappa}{\tilde{\sigma}_r^2} \exp\left(-\frac{\kappa J_r}{\tilde{\sigma}_r^2}\right) \times \frac{v}{\tilde{\sigma}_z^2} \exp\left(-\frac{v J_z}{\tilde{\sigma}_z^2}\right) \times \mathcal{L}, \quad (8)$$

$$\mathcal{L}(J_\phi) \equiv \begin{cases} 1 & \text{if } J_\phi \geq 0, \\ \exp\left(\frac{2\Sigma J_\phi}{\tilde{\sigma}_r^2}\right) & \text{if } J_\phi < 0. \end{cases} \quad (9)$$

$$\tilde{\Sigma}(R_c) \equiv \Sigma_0 \exp(-R_c/R_d), \quad (10)$$

$$\tilde{\sigma}_r^2 \equiv \tilde{\Sigma}_0 \exp(-2R_c/R_{\sigma,r}) + \sigma_{\min}^2, \quad (11)$$

$$\tilde{\sigma}_z^2 \equiv \Sigma_0 \exp(-2R_c/R_{\sigma,z}) + \sigma_{\min}^2, \quad (12)$$

with overall normalization $\tilde{\Sigma}_0$ of the surface density profile. R_d is the disc scale length. The radial velocity dispersion profile is nearly exponential in radius with central value $\sigma_{r,0}$, and radial scale length $R_{\sigma,r}$. The vertical velocity dispersion is also nearly exponential in radius, with central value $\sigma_{z,0}$, and radial scale $R_{\sigma,z}$. σ_{\min} is the minimum value of velocity dispersion, added in quadrature to both $\tilde{\sigma}_r$ and $\tilde{\sigma}_z$ to allow sensible behaviour at $J_r = J_z = 0$ and large J_ϕ . R_c is the radius of the circular orbit with angular momentum J_ϕ .

We generate a sample of 100 000 stars from the Milky-Way model and assign an arbitrary velocity error of 0.5 km s⁻¹ to each coordinate of every star's velocity. We recalculate a robust vertical velocity dispersion profile for stars between an absolute vertical height of 0.6 and 1.0 kpc, as for the stars in plot (b) of Fig. 4, leaving a sample of 12 344 stars. We modify the parameters of the DF in Piffl et al. (2014), which was fit to data for stars in the Solar Neighbourhood, until we roughly recover the vertical velocity dispersion profile observed for the primary RC stars younger than 6 Gyr. We assume the vertical velocity dispersion profile of stars younger than 6 Gyr reflects the vertical velocity dispersion profile of the older stars before the impact with the satellite. The selected DF parameters are given in Table 2. Fig. 5 shows the vertical velocity dispersion profile of the mock Milky Way model compared to the vertical velocity dispersion profiles by age for the primary RC stars.

4.2 Scattering by a Plummer sphere

To determine the velocity kicks imparted to a star in the Milky Way, we consider the scattering impact of a Plummer sphere. We will make the impulse approximation (Chew & Wick 1952), which is appropriate in situations where external forces on the system are

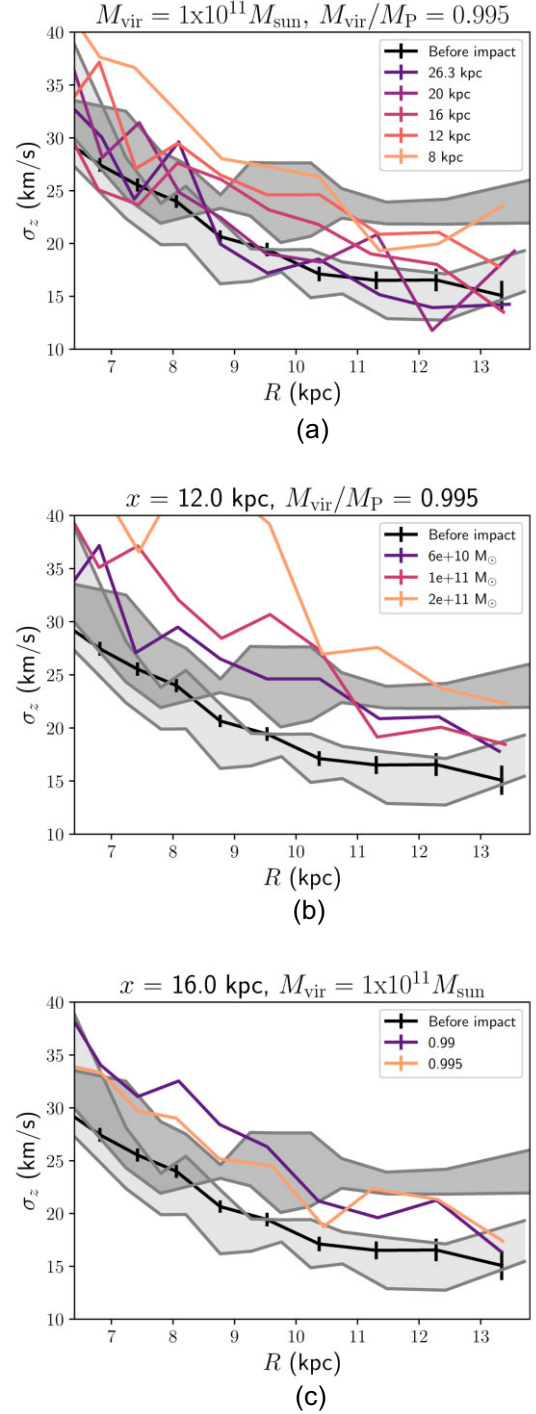


Figure 5. Robust vertical velocity dispersion profiles for stars younger than 6 Gyr (light grey region), stars older than 6 Gyr (dark grey region), the mock Milky Way model (solid black line), and the mock Milky Way model heated by impacts with (a) an object of virial mass $1 \times 10^{11} M_\odot$, virial mass to Plummer mass ratio of 0.995, and the x component of the impact parameter between 8 and 26.3 kpc; (b) an object of virial mass between 6×10^{10} and $2 \times 10^{11} M_\odot$, virial mass to Plummer mass ratio of 0.995, and $x = 12$ kpc; and (c) an object of virial mass $1 \times 10^{11} M_\odot$, virial mass to Plummer mass ratio of 0.99 and 0.995, and $x = 16$ kpc.

present, but they are small compared to the large, brief internal forces between parts of the system. The gravitational potential of the Plummer sphere, Φ , is given by:

$$\Phi(r) = \frac{GM_0}{\sqrt{r^2 + r_s^2}}, \quad (13)$$

where G is the gravitational constant, M_0 is the mass of the satellite, r_s is the scale radius of the satellite, and $r^2 = (x^2 + y^2 + z^2)$. (x, y, z) is the displacement vector between the star and the satellite.

(b_x, b_y, b_z) is the displacement vector at the point of closest approach between the star and the satellite, and (w_x, w_y, w_z) is the relative velocity at that point. Making this point, the zero-point in time, $x_i = b_i + w_i t$, where $i = x, y, z$. Note that $\vec{b} \cdot \vec{w} = 0$, $b^2 = \sum_i b_i^2$, and $w^2 = \sum_i w_i^2$.

The acceleration a_i felt by the disc star is given by

$$a_i = \frac{d\Phi}{dx_i} \quad (14)$$

$$= \frac{GM_0 x_i}{r_s^2 + \sum_i x_i^2} \quad (15)$$

$$= \frac{GM_0(b_i + w_i t)}{[r_s^2 + \sum_i (b_i + w_i t)^2]^{3/2}} \quad (16)$$

$$= \frac{GM_0(b_i + w_i t)}{[r_s^2 + \sum_i (b_i^2 + w_i^2 t^2)]^{3/2}} \quad (17)$$

$$= \frac{GM_0(b_i + w_i t)}{(r_s^2 + b^2 + w^2 t^2)^{3/2}} \quad (18)$$

Defining $\chi^2 \equiv r_s^2 + b^2$, the resulting velocity kick is then given by

$$\begin{aligned} \Delta v_i &= \int_{-\infty}^{\infty} a_i dt \\ &= \int_{-\infty}^{\infty} \frac{GM_0(b_i + w_i t)}{(\chi^2 + w^2 t^2)^{3/2}} dt \\ &= GM_0 \left(\frac{b_i}{w^3} \int_{-\infty}^{\infty} \frac{1}{(\frac{\chi^2}{w^2} + t^2)^{3/2}} dt + \frac{w_i}{w^3} \int_{-\infty}^{\infty} \frac{t}{(\frac{\chi^2}{w^2} + t^2)^{3/2}} dt \right) \\ &= GM_0 \left[\frac{b_i}{w^3} \left(\frac{t}{\frac{\chi^2}{w^2} (\frac{\chi^2}{w^2} + t^2)^{1/2}} \right) - \frac{w_i}{w^3} \left(\frac{\chi^2}{w_i^2} + t^2 \right)^{-1/2} \right]_{-\infty}^{\infty} \\ &= \frac{2GM_0 b_i}{w\chi^2}. \end{aligned} \quad (19)$$

The result is a simple expression for the velocity kick.

4.3 Simulated vertical velocity dispersion profiles following impact

To simulate the potential impact of a satellite on the outer thin disc of the Milky Way, we explore the possibility that the impact 6 Gyr ago was with a Plummer-sphere-like object. Vasiliev & Belokurov (2020) perform a number of N -body simulations of a disrupting Sgr galaxy as it orbits the Milky Way over the past 2.5 Gyr, tailored to reproduce the observed properties of the remnant as measured by the second data release from *Gaia* (Gaia Collab. et al. 2018) and line-of-sight velocities from other surveys. At the last pericentric passage, they find a relative velocity between the satellite and the Milky Way of $w_{\text{Sag-MW}} = (-45.82, -93.79, 255.52) \text{ km s}^{-1}$, and impact parameter $b_{\text{Sag-MW}} = (26.27, -0.821, -1.397) \text{ kpc}$. Here, we assume the same relative velocity and impact parameter, but additionally consider $x = 8, 12, 16, \text{ and } 20 \text{ kpc}$. We explore virial masses similar to that explored for the progenitor Sgr in Laporte et al. (2018), in their exploration

of the influence of Sgr and the Large Magellanic Cloud (LMC) on the stellar disc of the Milky Way. Specifically, we explore virial masses of $6 \times 10^{10}, 1 \times 10^{11}$, and $2 \times 10^{11} M_{\odot}$. We also explore different concentrations, assuming the virial mass is 0.99 and 0.995 of the Plummer mass. This corresponds to different scale radii of the Plummer sphere. We ran $5 \times 3 \times 2 = 30$ simulations in total.

We use equation (19) to derive the velocity kicks given the impact parameters for a random sample of 10 000 stars from the 100 000 in our mock sample. We then relax the 10 000 stars for approximately two dynamical timescales (evaluated for the outer disc), about 4 Gyr. We recalculate a robust vertical velocity dispersion profile and re-select stars between an absolute vertical height of 0.6 and 1.0 kpc.

Fig. 5 shows a selection of these results. (a) shows the effect of the impact parameter (in terms of the x coordinate) for a virial mass $1 \times 10^{11} M_{\odot}$ and a virial mass to Plummer mass ratio of 0.995. The closer the object to the centre of the Milky Way, the bigger the effect on the vertical velocity dispersion, especially within the solar radius. Increasing the mass of the object (see (b)) also increases the effect, in particular within the solar radius. Increasing the concentration (see (c)) appears to steepen the effect with radius. The simulations that most closely recovered the vertical velocity dispersion of primary RC stars beyond the Galactic Plane older than 6 Gyr were the models with a virial mass of $6 \times 10^{10} M_{\odot}$, $x = 12 \text{ kpc}$, and a virial mass to Plummer mass ratio of 0.995 (shown in Fig. 5 (b)), and a virial mass of $1 \times 10^{11} M_{\odot}$, $x = 16 \text{ kpc}$, and a virial mass to Plummer mass ratio of 0.995 (shown in Fig. 5 (a)).

5 DISCUSSION

Here, we discuss other interpretations of the chrono-chemodynamical structure of the outer disc, the evidence supporting Sgr as the massive satellite in the case such a scenario is the correct one, and limitations in the analysis.

5.1 Other interpretations of the chrono-chemodynamical structure of the outer disc

There are other possible interpretations of the chrono-chemodynamical structure in the outer disc of the Milky Way. An abrupt jump in the vertical velocity dispersion profile at 6 Gyr is unlikely to be the result of background heating by giant molecular clouds (GMCs) or dark matter subhaloes, as these occur continuously, resulting in a smoother heating effect (see e.g. Aumer, Binney & Schönrich 2016). Radial migration from the inner disc is also an unlikely explanation. It is unclear whether the velocity dispersion of the radially-migrated stars should be higher (e.g. Vera-Ciro et al. 2014) and why the effect would only be discernible for stars older than 6 Gyr. The radially-migrated stars should be metal richer too.

The scenario proposed in Renaud et al. (2021b), where the outer gas disc is fed by a separate gas filament to that feeding the inner gas disc, is a possibility. The outer gas disc is initially misaligned with respect to the inner gas disc. Stars form in the outer disc after a significant minor merger event, and then the discs align resulting in a hot outer disc. In this scenario, however, the stars born in the outer disc at the time of the significant minor merger event should be the kinematically hot stars. In the RC sample, all stars beyond the Solar Neighbourhood, beyond the Galactic plane, and older than 6 Gyr, are hot, even though the overdensity in $[\text{Fe}/\text{H}]$, $[\alpha/\text{Fe}]$, and τ appears to be centred at around 7 Gyr.

The scenario in which a massive satellite produced the jump in the vertical velocity dispersion profiles at 6 Gyr is supported by simu-

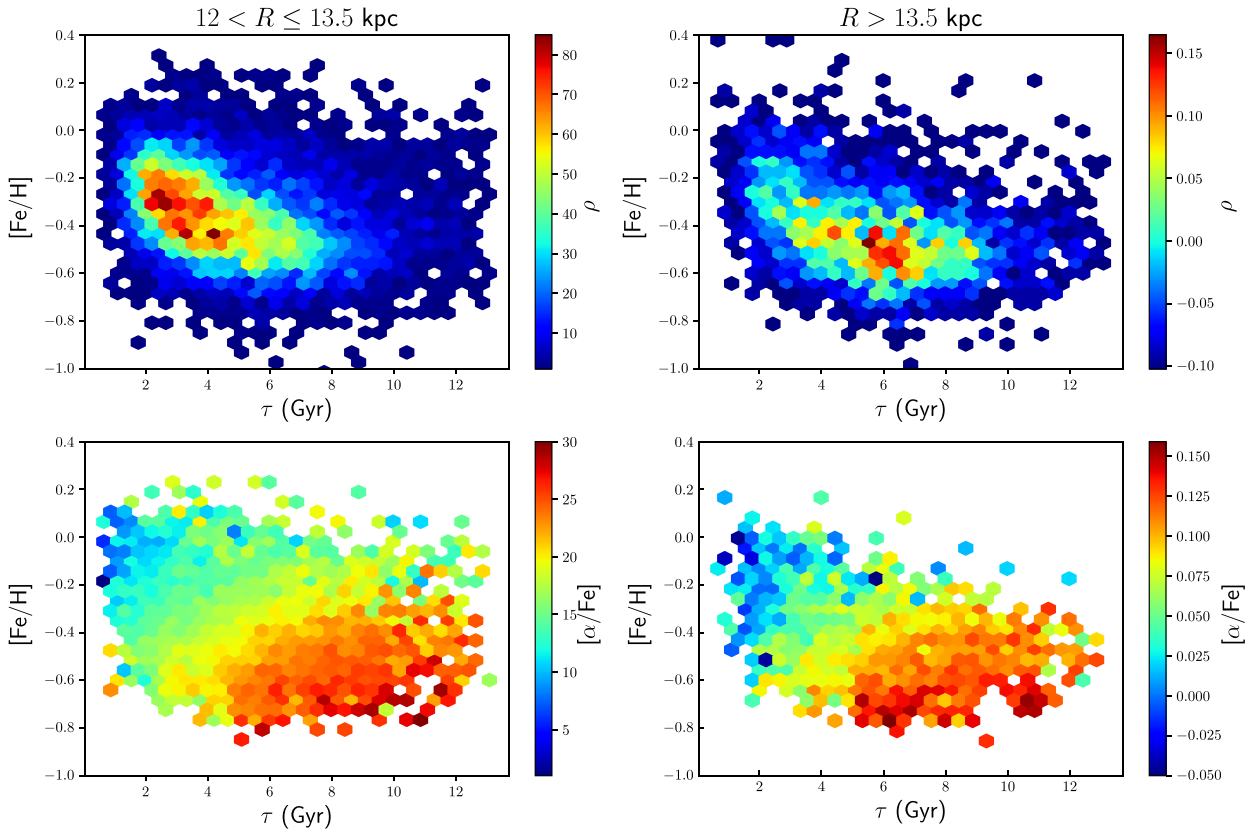


Figure 6. Hexbin plots of the low- α primary RC sample in the $[\text{Fe}/\text{H}]-\tau$ plane for stars between 12 and 13.5 kpc (left-hand panel) and beyond 13.5 kpc (right-hand panel) in density (top) and $[\alpha/\text{Fe}]$ (bottom). Note the overdensity at ~ 7 Gyr and $[\text{Fe}/\text{H}] \sim -0.5$ in the density map for stars beyond 13.5 kpc and the faint streak towards lower $[\text{Fe}/\text{H}]$ and higher $[\alpha/\text{Fe}]$ just under the overdensity.

lations ran by Martig, Minchev & Flynn (2014b). They studied the relation between stellar ages and vertical velocity dispersion (age–velocity dispersion relation, AVR) in a sample of seven simulated disc galaxies. They found that the shape of the AVR for stars younger than 9 Gyr depended strongly on the merger history at low redshift, with even 1:10 to 1:15 mergers being able to create jumps in the AVR (these jumps may not be visible if age errors are $\gtrsim 30$ per cent). The additional finding of an overdensity in the $[\text{Fe}/\text{H}]$, $[\alpha/\text{Fe}]$, τ hyperplane, suggesting a starburst induced by the pericentric passage of the massive satellite, further supports this scenario.

Mergers and pericentric passages of satellites can bring metal-poorer gas that dilutes the pre-existing gas (Grand et al. 2020; Renaud et al. 2021a). New stars that form would be metal poorer than expected. Pre-existing metal-poor stars born in the shallower satellite potential could also be deposited in the host. Both scenarios should produce a dip towards lower metallicities at the same age in the $[\text{Fe}/\text{H}]-\tau$ plane (Renaud et al. 2021a; Ciucă et al. 2022). Fig. 6 zooms into the $[\text{Fe}/\text{H}]-\tau$ plane for stars just within and beyond 13.5 kpc. The density map beyond 13.5 kpc shows a clear overdensity at ages just below 7 Gyr, and metallicities around -0.5 , corresponding to the metal-poor, α -rich, component that emerges in the very outer disc in Fig. 3. There is very tentative evidence for a streak towards lower metallicities around the same age. The bottom panels show the $[\alpha/\text{Fe}]$ maps in this plane. The faint streak beyond 13.5 kpc is also higher in $[\alpha/\text{Fe}]$. Looking at Fig. 8 in Feltzing, Bowers & Agertz (2020), one can see the expected metallicity of non-radially migrated stars by Galactocentric radii and age. Extrapolating out to 13.5 kpc, one

can see that the youngest disc stars should have a metallicity of ~ -0.4 , and the oldest disc stars should have a metallicity of ~ -0.6 . Therefore, the overdensity at ~ 7 Gyr and a metallicity of ~ -0.5 were likely born from pre-existing gas that belongs to the MW. The streak towards lower metallicities could be from metal-poorer gas brought in by a massive satellite.

5.2 The possibility of Sgr as the massive satellite perturber

We find that an object of mass $\sim 10^{11}$ is required to produce the observed jump in vertical velocity dispersion at 6 Gyr for primary RC stars above and below the Galactic plane, assuming the object had the same relative velocity, y , and z coordinates as Sgr at its last pericentric passage (Vasiliev & Belokurov 2020), but $x = 12$ to 16 kpc.

Many attempts exist in the literature at estimating the progenitor mass of Sgr. Niederste-Ostholt et al. (2010) reassemble the stellar debris using Sloan Digital Sky Survey (SDSS) and Two Micron All-Sky Survey data to estimate a mass for Sgr’s dark matter halo, prior to tidal disruption, of $\sim 10^{10} M_{\odot}$. Gibbons, Belokurov & Evans (2017) use SDSS stars in the leading and trailing streams of Sgr to demonstrate the existence of two subpopulations with distinct chemistry and kinematics. They show that the dark halo of Sgr must have been $\gtrsim 6 \times 10^{10} M_{\odot}$ to reproduce the observed velocity dispersions. Mucciarelli et al. (2017) attempt to reproduce the observed chemical patterns of Sgr and conclude that the total progenitor mass is $6 \times 10^{10} M_{\odot}$. Laporte et al. (2018, 2019) analyse

an N -body simulation of the interaction of the Milky Way with a Sgr-like galaxy and are able to explain a remarkable number of signs of perturbations in the Milky Way, when assuming a progenitor Sgr with a mass of $\sim 6 \times 10^{10} M_{\odot}$. These include overdensities such as the Monoceros Ring (Newberg et al. 2002) and the Anti-Center Stream, (Grillmair 2006), and the phase-space spiral observed in the *Gaia* DR2 data (Antoja et al. 2018). The estimate we derive here is very similar to these previous estimates in the literature.

Laporte et al. (2019) time the relevant interaction with Sagittarius to be 500 to 800 Myr ago. Evidence for the most recent interaction is also presented in Ruiz-Lara et al. (2020), who analyse *Gaia* DR2 colour-magnitude diagrams to obtain a detailed star formation history in a ~ 2 kpc bubble around the Sun. Their study revealed a narrow episode of enhanced star formation at 1.0 Gyr ago, and also at 1.9 and 5.7 Gyr ago. The most ancient interaction they find is at a similar time to that found in the work here. We still need to understand, however, how a starburst might propagate from the outer disc to the inner disc and how far we expect such a starburst to propagate.

For a system, the size of our Milky Way ($\sim 10^{12} M_{\odot}$, e.g. Craig et al. (2022)), the cut-off model in Fig. 3 of Santos-Santos et al. (2022) suggests that we expect ~ 3 satellites with a stellar mass of $10^8 M_{\odot}$, and ~ 1 satellite with a stellar mass of $10^9 M_{\odot}$. Using Fig. 3 in Read & Erkal (2019), we can map these stellar masses to total masses of $\sim 10^{10}$ and $\sim 10^{11} M_{\odot}$. The fact that there is a LMC, which may have a mass up to $\sim 10^{11} M_{\odot}$ as well as Sgr, also with a mass up to $\sim 10^{11} M_{\odot}$ is already unusual. It is very unlikely that yet another massive satellite exists in the halo of the Milky Way. The LMC is around 50 kpc (Pietrzyński et al. 2013) from the centre of the Milky Way, which is too far away to have the observed effect on the vertical velocity dispersion. This only leaves Sgr as the possible candidate.

The pericentric radius inferred in this work 6 Gyr ago is between 12 and 16 kpc. This is closer than the 26.3 kpc found for the last pericentric passage of Sgr in Vasiliev & Belokurov (2020). This is unexpected as one expects large satellites to sink towards the centre of the host galaxy due to dynamical friction. However, recent work analysing the orbital dynamics and histories of satellite galaxies around Milky Way (MW)-mass host galaxies in the FIRE-2 cosmological simulations found that for 67 per cent of the satellites, the most recent pericentre was not their minimum pericentre (Santistevan et al. 2023). The minimum typically was 40 per cent smaller and occurred ~ 6 Gyr earlier, possibly coincidentally, very similar to what we find here. They attribute the increasing pericentres to a combination of a time-dependent Milky-Way-mass halo potential and dynamical perturbations in the outer halo.

The metallicity distribution function (MDF) of current stars identified to belong to the core remnant of Sagittarius (e.g. Minelli et al. 2023) finds an MDF that peaks at -0.5 with an extended tail reaching $[\text{Fe}/\text{H}] \lesssim -2.0$. The gas that has already been stripped from Sagittarius is likely to be on the metal poorer end. Therefore the streak towards lower metallicities observed in Fig. 6 could have been brought in by Sagittarius.

6 CONCLUSIONS AND FURTHER WORK

A primary RC sample drawn from the 4th data release of LAMOST was used to examine the chrono-chemodynamical structure of the Milky Way, with a focus on the outer disc. The vertical velocity dispersion profiles by age for stars beyond the Solar Neighbourhood, and beyond the Galactic plane, show a jump at 6 Gyr. The chemistry and age histograms reveal a bump at $[\text{Fe}/\text{H}] = -0.5$, $[\alpha/\text{Fe}] = 0.1$, and an age of 7.2 Gyr, and stars beyond 13.5 kpc show a dip in metallicity just below the bump. These data suggest that a massive satellite had

a close encounter with the Milky Way ~ 6 Gyr ago, heating all pre-existing stars, causing a starburst, and bringing in metal-poorer gas that subsequently formed stars. The impulse approximation was used to weigh and determine the orbit of the massive satellite, finding a mass $\sim 10^{11} M_{\odot}$ and a pericentric radius between 12 and 16 kpc. The massive satellite is likely to be Sgr.

The work shows the potential for the second-order moments of velocity to encode more ancient interactions with massive satellites (rather than the first-order velocity moments that encode more recent interactions, e.g. Laporte et al. (2019)).

The second paper in the series will address a key uncertainty in the analysis presented here. The starburst in the outer disc was found to be centred at ~ 7 Gyr and $[\text{Fe}/\text{H}] \sim -0.5$. The primary RC clump sample has a strong sample selection function due to the selection in colour and metallicity. This will result in a bias in the distance-metallicity-age distribution of the stars that needs to be accounted for to correctly position the starburst in the age-metallicity plane. The second paper presents an extended distribution function model for the outer disc that takes the selection function into account.

The second uncertainty in the analysis presented here is in the application of the impulse approximation to estimate the orbital parameters of the satellite. The impulse approximation assumes that the dynamical heating effect is dominated by the velocity kicks imparted on the disc stars by the satellite at the point of closest approach. In future work, we will run N -body simulations to follow this impact and explore a wider parameter space.

ACKNOWLEDGEMENTS

PD is supported by a UKRI Future Leaders Fellowship (grant reference MR/S032223/1). YH is supported by National Key R&D Program of China No. 2019YFA0405500 and National Natural Science Foundation of China grants 11903027 and 11833006. PD would also like to thank the anonymous reviewer, and Mr David Hendriks at the University of Surrey, for a thorough read of the manuscript.

This work has made use of data from the European Space Agency (ESA) mission *Gaia* (<https://www.cosmos.esa.int/gaia>), processed by the *Gaia* Data Processing and Analysis Consortium (DPAC, <https://www.cosmos.esa.int/web/gaia/dpac/consortium>). Funding for the DPAC has been provided by national institutions, in particular the institutions participating in the *Gaia* Multilateral Agreement.

The Guoshoujing Telescope (the Large Sky Area Multi-Object Fiber Spectroscopic Telescope, LAMOST) is a National Major Scientific Project built by the Chinese Academy of Sciences. Funding for the project has been provided by the National Development and Reform Commission. LAMOST is operated and managed by the National Astronomical Observatories, Chinese Academy of Sciences. The LAMOST FELLOWSHIP is supported by Special fund for Advanced Users, budgeted and administrated by Center for Astronomical Mega-Science, Chinese Academy of Sciences (CAMS).

DATA AVAILABILITY

The red clump sample analysed in this article is publicly available at <https://zenodo.org/deposit/3875974>. The code and data generated to produce the figures, and the code and simulation data generated in the impulse approximation models will be shared on reasonable request to the corresponding author.

REFERENCES

- Amôres E. B., Robin A. C., Reylé C., 2017, *A&A*, 602, A67
- Antoja T. et al., 2018, *Nature*, 561, 360
- Arenou F. et al., 2018, *A&A*, 616, A17
- Aumer M., Binney J., Schönrich R., 2016, *MNRAS*, 462, 1697
- Bovy J., Rix H.-W., Schlafly E. F., Nidever D. L., Holtzman J. A., Shetrone M., Beers T. C., 2016, *ApJ*, 823, 30
- Brent R. P., 2013, Algorithms for minimization without derivatives. Courier Corporation, Chelmsford, Massachusetts, United States
- Chew G. F., Wick G. C., 1952, *Phys. Rev.*, 85, 636
- Chiang B. T., Ostriker J. P., Schive H.-Y., 2023, *MNRAS*, 518, 4045
- Church B. V., Mocz P., Ostriker J. P., 2019, *MNRAS*, 485, 2861
- Ciucă I., Kawata D., Miglio A., Davies G. R., Grand R. J. J., 2021, *MNRAS*, 503, 2814
- Ciucă I. et al., 2022, *MNRAS*, in press, preprint (arXiv:2211.01006)
- Craig P. A., Chakrabarti S., Baum S., Lewis B. T., 2022, *MNRAS*, 517, 1737
- García de la Cruz J., Martig M., Minchev I., James P., 2020, *MNRAS*, 501, 5105
- Das P., Sanders J. L., 2019, *MNRAS*, 484, 294
- Feltzing S., Bowers J. B., Agertz O., 2020, *MNRAS*, 493, 1419
- Gaia Collab. et al., 2016, *A&A*, 595, A1
- Gaia Collab. et al., 2018, *A&A*, 616, A1
- Gaia Collab. et al., 2021, *A&A*, 649, A1
- Gibbons S. L. J., Belokurov V., Evans N. W., 2017, *MNRAS*, 464, 794
- Gómez F. A., Minchev I., O’Shea B. W., Beers T. C., Bullock J. S., Purcell C. W., 2013, *MNRAS*, 429, 159
- Grand R. J. J. et al., 2020, *MNRAS*, 497, 1603
- Grillmair C. J., 2006, *ApJ*, 651, L29
- Horta D. et al., 2023, *MNRAS*, 520, 5671
- Huang Y. et al., 2020, *ApJS*, 249, 29
- Kazantzidis S., Zentner A. R., Kravtsov A. V., Bullock J. S., Debattista V. P., 2009, *ApJ*, 700, 1896
- Kordopatis G. et al., 2023, *A&A*, 669, A104
- Laporte C. F. P., Johnston K. V., Gómez F. A., Garavito-Camargo N., Besla G., 2018, *MNRAS*, 481, 286
- Laporte C. F. P., Minchev I., Johnston K. V., Gómez F. A., 2019, *MNRAS*, 485, 3134
- Laporte C. F. P., Belokurov V., Koposov S. E., Smith M. C., Hill V., 2020, *MNRAS*, 492, L61
- Laporte C. F. P., Koposov S. E., Belokurov V., 2022, *MNRAS*, 510, L13
- Lindgren L. et al., 2018, *A&A*, 616, A2
- Mackereth J. T. et al., 2017, *MNRAS*, 471, 3057
- Martig M., Minchev I., Flynn C., 2014a, *MNRAS*, 442, 2474
- Martig M., Minchev I., Flynn C., 2014b, *MNRAS*, 443, 2452
- McMillan P. J., 2017, *MNRAS*, 465, 76
- Minchev I., Famaey B., Quillen A. C., Di Matteo P., Combes F., Vlahić M., Erwin P., Bland-Hawthorn J., 2012a, *A&A*, 548, A126
- Minchev I., Famaey B., Quillen A. C., Dehnen W., Martig M., Siebert A., 2012b, *A&A*, 548, A127
- Minelli A. et al., 2023, *A&A*, 669, A54
- Mints, Alexey, 2018, preprint (arXiv:1805.01640)
- Mucciarelli A., Bellazzini M., Ibata R., Romano D., Chapman S. C., Monaco L., 2017, *A&A*, 605, A46
- Newberg H. J. et al., 2002, *ApJ*, 569, 245
- Niederste-Ostholt M., Belokurov V., Evans N. W., Peñarrubia J., 2010, *ApJ*, 712, 516
- Pietrzyński G. et al., 2013, *Nature*, 495, 76
- Piffl T. et al., 2014, *MNRAS*, 445, 3133
- Queiroz A. B. A. et al., 2018, *MNRAS*, 476, 2556
- Read J. I., Erkal D., 2019, *MNRAS*, 487, 5799
- Renaud F., Agertz O., Read J. I., Ryde N., Andersson E. P., Bensby T., Rey M. P., Feuillet D. K., 2021a, *MNRAS*, 503, 5846
- Renaud F., Agertz O., Andersson E. P., Read J. I., Ryde N., Bensby T., Rey M. P., Feuillet D. K., 2021b, *MNRAS*, 503, 5868
- Ruiz-Lara T., Gallart C., Bernard E. J., Cassisi S., 2020, *New A*, 4, 965
- Sanders J. L., Das P., 2018, *MNRAS*, 481, 4093
- Santistevan I. B., Wetzell A., Tollerud E., Sanderson R. E., Samuel J., 2023, *MNRAS*, 518, 1427
- Santos-Santos I. M. E., Sales L. V., Fattahi A., Navarro J. F., 2022, *MNRAS*, 515, 3685
- Sellwood J. A., Binney J. J., 2002, *MNRAS*, 336, 785
- Sharma S. et al., 2021, *MNRAS*, 506, 1761
- Sun W. -X. et al., 2020, *ApJ*, 903, 12
- Thomas G. F. et al., 2019, *MNRAS*, 483, 3119
- Vasiliev E., 2019, *MNRAS*, 482, 1525
- Vasiliev E., Belokurov V., 2020, *MNRAS*, 497, 4162
- Velazquez H., White S. D. M., 1999, *MNRAS*, 304, 254
- Vera-Ciro C., D’Onghia E., 2016, *ApJ*, 824, 39
- Vera-Ciro C., D’Onghia E., Navarro J., Abadi M., 2014, *ApJ*, 794, 173
- Yu Z. et al., 2021, *ApJ*, 912, 106

This paper has been typeset from a $\text{\TeX}/\text{\LaTeX}$ file prepared by the author.